

## Inflight radiometric calibration of New Horizons' Multispectral Visible Imaging Camera (MVIC)



C.J.A. Howett<sup>a,\*</sup>, A.H. Parker<sup>a</sup>, C.B. Olkin<sup>a</sup>, D.C. Reuter<sup>b</sup>, K. Ennico<sup>c</sup>, W.M. Grundy<sup>d</sup>, A.L. Graps<sup>e,f</sup>, K.P. Harrison<sup>g</sup>, H.B. Throop<sup>h</sup>, M.W. Buie<sup>a</sup>, J.R. Lovering<sup>i</sup>, S.B. Porter<sup>a</sup>, H.A. Weaver<sup>j</sup>, L.A. Young<sup>a</sup>, S.A. Stern<sup>a</sup>, R.A. Beyer<sup>c</sup>, R.P. Binzel<sup>k</sup>, B.J. Buratti<sup>l</sup>, A.F. Cheng<sup>j</sup>, J.C. Cook<sup>a</sup>, D.P. Cruikshank<sup>c</sup>, C.M. Dalle Ore<sup>c</sup>, A.M. Earle<sup>k</sup>, D.E. Jennings<sup>b</sup>, I.R. Linscott<sup>m</sup>, A.W. Lunsford<sup>b</sup>, J.W.m. Parker<sup>a</sup>, S. Phillippe<sup>n</sup>, S. Protopapa<sup>o</sup>, E. Quirico<sup>n</sup>, P.M. Schenk<sup>p</sup>, B. Schmitt<sup>n</sup>, K.N. Singer<sup>a</sup>, J.R. Spencer<sup>a</sup>, J.A. Stansberry<sup>q</sup>, C.C.C. Tsang<sup>a</sup>, G.E. Weigle II<sup>r</sup>, A.J. Verbiscer<sup>s</sup>

<sup>a</sup>Southwest Research Institute, Boulder, CO 80302, USA

<sup>b</sup>NASA Goddard Space Flight Center, Greenbelt, MD 20771, USA

<sup>c</sup>NASA Ames Research Center, Space Science Division, Moffett Field, CA 94035, USA

<sup>d</sup>Lowell Observatory, Flagstaff, AZ 86001, USA

<sup>e</sup>Planetary Science Institute, Riga, Latvia

<sup>f</sup>University of Latvia, Riga, Latvia

<sup>g</sup>Consultant, Denver, CO, USA

<sup>h</sup>Planetary Science Institute, Mumbai, India

<sup>i</sup>The Breakthrough Institute, Oakland, CA 94612, USA

<sup>j</sup>Johns Hopkins University Applied Physics Laboratory, Laurel, MD 20723, USA

<sup>k</sup>Massachusetts Institute of Technology, Cambridge, MA 02139, USA

<sup>l</sup>NASA Jet Propulsion Laboratory, La Cañada Flintridge, CA 91011, USA

<sup>m</sup>Stanford University, Stanford CA 94305, USA

<sup>n</sup>Université Grenoble Alpes, CNRS, IPAG, F-38000 Grenoble, France

<sup>o</sup>Department of Astronomy, University of Maryland, College Park, MD 20742, USA

<sup>p</sup>Lunar and Planetary Institute, Houston, TX 77058, USA

<sup>q</sup>Space Telescope Science Institute, Baltimore, MD 21218, USA

<sup>r</sup>Southwest Research Institute, San Antonio, TX 28510, USA

<sup>s</sup>Department of Astronomy, University of Virginia, Charlottesville, VA 22904, USA

### ARTICLE INFO

#### Article history:

Received 15 March 2016

Revised 19 November 2016

Accepted 3 December 2016

Available online 6 December 2016

#### Keywords:

Image processing

Pluto, surface

Charon

### ABSTRACT

We discuss two semi-independent calibration techniques used to determine the inflight radiometric calibration for the New Horizons' Multi-spectral Visible Imaging Camera (MVIC). The first calibration technique compares the measured number of counts (DN) observed from a number of well calibrated stars to those predicted using the component-level calibration. The ratio of these values provides a multiplicative factor that allows a conversation between the preflight calibration to the more accurate inflight one, for each detector. The second calibration technique is a channel-wise relative radiometric calibration for MVIC's blue, near-infrared and methane color channels using Hubble and New Horizons observations of Charon and scaling from the red channel stellar calibration. Both calibration techniques produce very similar results (better than 7% agreement), providing strong validation for the techniques used. Since the stellar calibration described here can be performed without a color target in the field of view and covers all of MVIC's detectors, this calibration was used to provide the radiometric keyword values delivered by the New Horizons project to the Planetary Data System (PDS). These keyword values allow each observation to be converted from counts to physical units; a description of how these keyword values were generated is included. Finally, mitigation techniques adopted for the gain drift observed in the near-infrared detector and one of the panchromatic framing cameras are also discussed.

© 2016 Elsevier Inc. All rights reserved.

\* Corresponding author. Fax: +1 303-546-9687.

E-mail address: [howett@boulder.swri.edu](mailto:howett@boulder.swri.edu) (C.J.A. Howett).

## 1. Introduction

### 1.1. MVIC

The Multi-spectral Visible Imaging Camera (MVIC) is part of the Ralph instrument on the New Horizons spacecraft. Full details of the instrument can be found in Reuter et al. (2008), but an overview is provided here for reference. A single substrate holds MVIC's seven independent CCD arrays. Six of these CCDs operate in Time Delay and Integration mode (TDI), and each has  $5024 \times 32$  pixels. There are two panchromatic (Pan) TDI arrays with the same wavelength range for redundancy, and four other TDI arrays each with a color filter (Red, Blue, NIR, CH4). The final array is a frame transfer  $5024 \times 128$  pixel array, primarily designed for optical navigation. The Pan TDI arrays can be operated between 4 and 84 Hz, while the color TDI rates are between 4 and 54 Hz. The frame transfer integration time can vary between 0.25 to 10 s. Further details of all these arrays can be found in Table 1.

TDI is a way of increasing the signal-to-noise ratio (SNR) while building up a large format pushbroom image as the field of view (FOV) is quickly scanned across a scene. It works by syncing the transfer rate between rows to the spacecraft's scan rate, thus the same scene passes through each of the rows before it is read out, effectively increasing the integration time. The frame transfer camera is operated in the more traditional stare mode.

Prelaunch calibration of MVIC consisted of two separate, but related, calibrations: the absolute radiometry of the instrument, and the characterization of its components (c.f. Reuter et al., 2008). MVIC's absolute radiometry was determined using an integrating sphere, but it was estimated that this calibration was only accurate to  $\pm 30\%$ , and that inflight radiometric calibration would be required (Reuter et al., 2008). This work reports the method and results of this inflight calibration.

At the component-level the quantum efficiency of MVIC's detectors ( $Q_e$ ), the filter transmission ( $F_f$ ) and the reflectance of both the beam splitter ( $B_S$ ) and the mirror ( $A_I$ ) were measured. These measurements can be combined according to Eq. (1) to define the response ( $\chi$ ) as a function of wavelength ( $\lambda$ ) for each of the MVIC's detectors. The mirror reflectance is cubed because there are three mirrors in the system.

$$\chi(\lambda) = Q_e(\lambda)F_f(\lambda)B_S(\lambda)A_I^3(\lambda), \quad (1)$$

Reuter et al. (2008) provided MVIC's quantum efficiencies and filter transmissions as measured before launch. Fig. 1 shows these values, along with the measured beam splitter reflectance and mirror reflectance. As the figure shows, when these values are combined to give a responsivity many of the color detectors have a larger response than either of the panchromatic detectors at some wavelengths. The ground-based spectral sampling of the detectors'  $Q_e$  values was very coarse ( $\sim 50$  nm), so it is possible these curves are not accurately characterized. A minor correction was made to restrict the peak of all the color detectors'  $Q_e$  values to that of the panchromatic detector, as it was deemed unlikely that their re-

sponse would be higher than that of the clear filter given the identical nature of all the CCDs (Reuter et al., 2008). This correction has an almost negligible effect on the final result, as the new calibration can be thought of as further correcting these values. The new pre-launch responsivities used in this work are also shown in Fig. 1. Using each filter's responsivity the effective (or pivot) wavelength  $\lambda_p$  for a given filter is calculated according to Eq. (2), where  $\chi$  and  $\lambda$  are defined as above (Laidler et al., 2005).

$$\lambda_p = \sqrt{\frac{\int \lambda \chi(\lambda) d\lambda}{\int (\chi(\lambda) d\lambda / \lambda)}} \quad (2)$$

### 1.2. Inflight calibration outline

This paper presents two parallel and semi-independent MVIC inflight radiometric calibration processes and one process for "bootstrapping" a correction for a gain drift identified in one of MVIC's two redundant sets of readout electronics. One radiometric calibration process, based on deriving system throughput corrections using photometry of calibration stars, is planned to become the long-term standard for MVIC calibration. The second radiometric calibration process is based on deriving corrections to the mean observed color ratios of Charon in order to match color ratios measured by the Hubble Space Telescope. It was developed for the Blue, Red, NIR, and CH4 MVIC channels on approach to the Pluto system to expedite a well-understood interim radiometric calibration solution in order to enable certain science observations (e.g., mapping the CH<sub>4</sub> ice distribution across Pluto using Red, NIR, and CH4 MVIC imagery; see Grundy et al., 2016). This Charon-based calibration was utilized by a number of the early New Horizons-based science papers (e.g., Grundy et al., 2016; Weaver et al., 2016). The following sections outline these calibration procedures, their results, and how the results of each procedure compare.

## 2. Stellar calibration

### 2.1. Calibration stellar observations

Each year during the 9.5 year cruise to the Pluto-Charon system the New Horizons spacecraft underwent an Annual Check-Out (ACO), with observations relevant to this work (i.e. observations of specific star clusters) taken every other year. Details of the observations used for the radiometric calibration of the Red, Blue, NIR, CH4, Pan 1, Pan 2 and Pan Frame cameras are given in Tables 2–5. As they show, most of the early observations (2008 to 2012) were of the Messier 6 and 7 clusters (NGC 6405 and 6475, or sometimes shortened to M6 and M7), while later observations (2013 to 2014) also included observations of the Wishing Well Cluster (NGC 3532). This change was made to include a larger number and variety of star types, to help with both the geometric distortion correction and radiometric calibration. An example of a typical image is shown in Fig. 2. The  $5.7^\circ$  field of view of MVIC is large enough to capture both the NGC 6405 and NGC 6475 clusters in a single image, which allows many stars to be observed simultaneously. All

**Table 1**

Details of the MVIC arrays. A single pixel is  $19.77 \mu\text{rad}$  by  $19.77 \mu\text{rad}$ , so the FOV of the TDI array is  $5.7^\circ$  by  $0.037^\circ$ , and that of the framing camera is  $5.7^\circ$  by  $0.146^\circ$ .

Array name	Array description	Wavelength range (nm)	Pivot wavelength (nm)	Array size (pixels)
Pan 1	Panchromatic TDI #1	400–975	692	$5024 \times 32$
Pan 2	Panchromatic TDI #2	400–975	692	$5024 \times 32$
Blue	Blue TDI	400–550	492	$5024 \times 32$
Red	Red TDI	540–700	624	$5024 \times 32$
NIR	Near-infrared TDI	780–975	861	$5024 \times 32$
CH4	Methane-Band TDI	860–910	883	$5024 \times 32$
Pan frame	Panchromatic framing camera	400–975	692	$5024 \times 128$

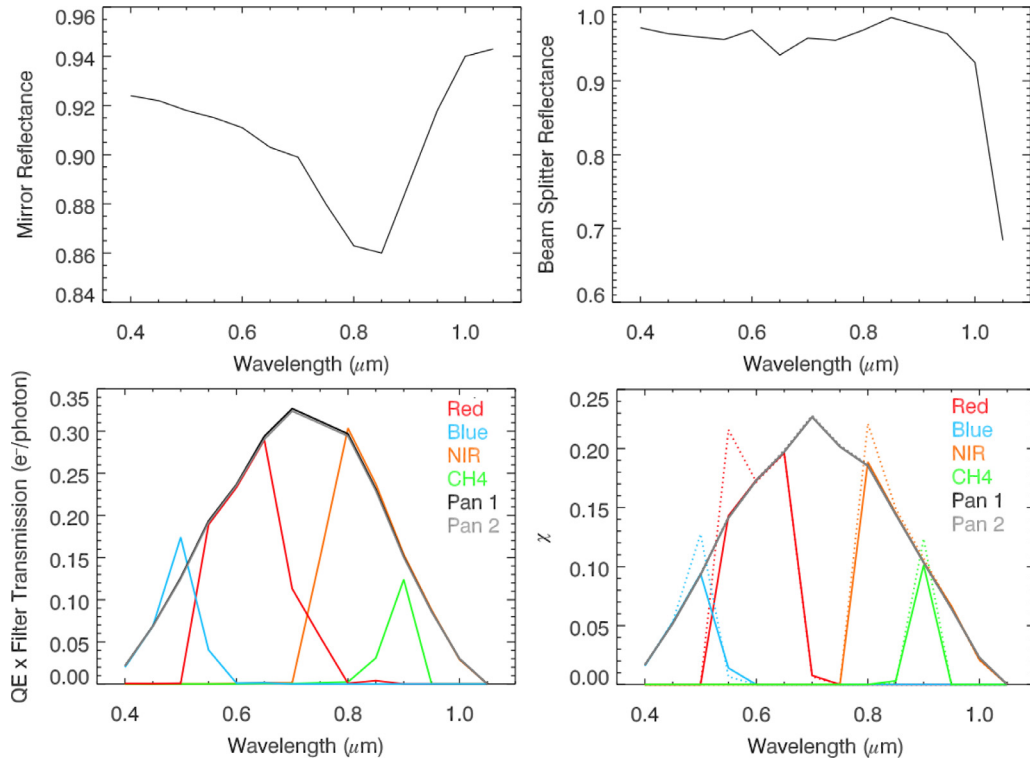


**Fig. 1.** Mirror and beamsplitter reflectance and the product of the quantum efficiency ( $Q_e$ ) and the different filter transmission curves are shown. These combine, as described in the main text, to produce the responsivity ( $\chi$ ). Both the original responsivity (dotted lines) and tweaked responsivity (solid lines) are shown. See main text for details.

**Table 2**

Details of the stellar observations used to calibrate the MVIC color channels (Red, Blue, NIR, CH4). All channels observed simultaneously.

Mid-observation time (UTC)	Onboard mission elapsed time (MET)	Right ascension (°)	Declination (°)	Exposure time (s)	Target
2008-10-15T04:45:25.191	0086351808	266.842	-33.457	2.919	NGC 6405 and 6475
2010-06-25T21:30:25.129	0139807309	266.767	-33.431	2.853	NGC 6405 and 6475
2012-06-01T21:15:25.784	0200891209	266.771	-33.434	2.880	NGC 6405 and 6475
2013-07-03T06:45:27.183	0235139809	166.433	-58.754	2.811	NGC 3532
2014-07-22T13:50:25.578	0268342909	266.859	-33.480	2.863	NGC 6405 and 6475
2014-07-22T13:57:19.578	0268343327	266.775	-33.371	4.244	NGC 6405 and 6475
2014-07-22T18:00:27.079	0268357909	166.433	-58.786	2.762	NGC 3532

**Table 3**

Details of the stellar observations made by Panchromatic Filter #1, used in this calibration.

Mid-observation time (UTC)	Onboard mission elapsed time (MET)	Right ascension (°)	Declination (°)	Exposure time (s)	Target
2008-10-15T05:00:11.691	0086352708	266.731	-33.471	2.891	NGC 6405 and 6475
2010-06-25T21:49:11.629	0139808449	266.780	-33.528	2.802	NGC 6405 and 6475
2012-06-01T21:32:11.284	0200892228	266.708	-33.461	2.828	NGC 6405 and 6475
2013-07-03T07:12:15.183	0235141429	166.391	-58.710	2.901	NGC 3532
2014-07-22T14:10:11.578	0268344108	266.732	-33.477	2.862	NGC 6405 and 6475
2014-07-22T18:15:14.579	0268358809	166.487	-58.685	2.762	NGC 3532

of the images used have been flat-fielded and bias-subtracted; the flat field used was calculated using results from ground-based and early-flight tests.

## 2.2. Overview of the modeling technique

The software written to perform this calibration was developed by many people, over many years. The basic premise of the software is to compare the flux observed by MVIC of a given star with a predicted model flux. If MVIC were perfectly calibrated the two would be identical, while any difference between them is the calibration offset this work seeks to determine. The offset for each of MVIC's detectors has to be separately determined.

## 2.3. Modeling the stellar flux

The first task is to find the stars in an MVIC image. Once this task is achieved the next steps are to determine which stars they are and then calculate the photon flux predicted from each star (to be compared eventually to the one observed). These first two steps are by far the most complicated aspect of the model, as it is possible to easily mistake hot-pixels as stars and miscorrelate stars with those cataloged.

The software finds all the potential stars in a given MVIC image by searching for bright pixels above a 5 data-number (DN) threshold value. It then uses the pointing information in the header to determine the Right Ascension (RA) and Declination (Dec) for each of these sources. The positions of all the stars are then compared

**Table 4**

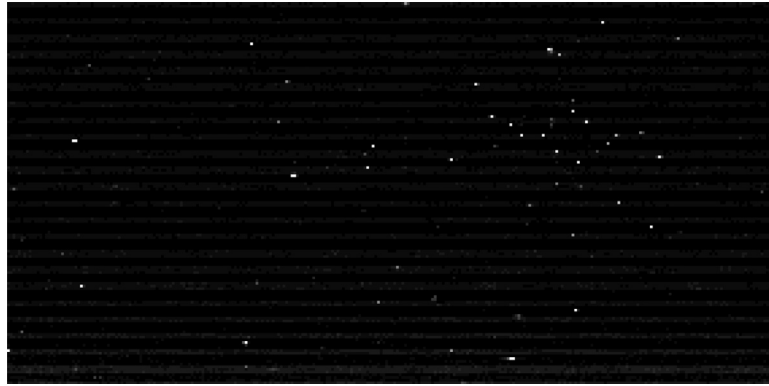
Details of the stellar observations made by Panchromatic Filter #2, used in this calibration.

Mid-observation time (UTC)	Onboard mission elapsed time (MET)	Right ascension (°)	Declination (°)	Exposure time (s)	Target
2008-10-15T04:52:11.691	086352228	266.764	−33.509	2.845	NGC 6405 and 6475
2010-06-25T21:40:11.629	0139807909	266.717	−33.505	2.766	NGC 6405 and 6475
2012-06-01T21:24:12.284	0200891749	266.753	−33.501	2.842	NGC 6405 and 6475
2013-07-03T07:03:15.183	0235140889	166.516	−58.730	2.902	NGC 3532
2014-07-22T18:07:15.079	0268358329	166.491	−58.720	2.850	NGC 3532

**Table 5**

Details of the stellar and planetary observations made by Panchromatic frame camera, used in this calibration. Each observation taken multiple times, as denoted by the number of frames.

Mid-observation time (UTC)	Onboard mission elapsed time (MET)	Right ascension (°)	Declination (°)	Exposure time (s)	# Frames	Target
2008-10-15T23:55:11.126	0086420815	346.135	−7.185	0.500	6	Neptune
2010-06-25T21:57:10.238	013.9808935	266.761	−33.531	1.000	5	NGC 6405 and 6475
2012-06-01T21:40:09.893	0200892714	266.838	−33.461	1.000	5	NGC 6405 and 6475
2012-06-02T01:28:10.393	0200906396	270.405	−14.638	0.500	5	Pluto
2012-06-02T01:28:34.663	0200906425	270.431	−14.636	1.000	2	Pluto
2013-07-02T19:30:10.291	0235099315	266.692	−33.506	1.000	5	NGC 6405 and 6475
2014-07-22T14:16:09.687	0268344474	266.785	−33.562	1.000	5	NGC 6405 and 6475
2014-07-23T17:15:06.535	0268441615	270.350	−14.444	1.000	3	Pluto
2014-07-23T17:23:05.535	0268442094	270.696	−14.635	1.000	3	Pluto

**Fig. 2.** MVIC red image from the M6/M7 cluster observations taken in 2014 (MET 0268342909).

to those in the Tycho-2 star catalog (Hog et al., 2000a,b), while those that are missing are assumed to either simply be missing from the Tycho catalog or are false-positives (for example cosmic ray strikes). The catalog provides each star's spectral type, Tycho V and B (referred to henceforth as  $B_T$  and  $V_T$  respectively) magnitudes, and temperature. From these values the Johnson V ( $V_J$ ) magnitude is determined for each star from the Tycho magnitudes, according to Hog et al. (2000c):  $V_J = V_T - 0.09 (B_T - V_T)$ .

The Kurucz 1993 Atlas (Kurucz, 1993) is used to determine the predicted spectral emission from each star using the Tycho catalog's stellar temperature and by assuming a solar abundance. The Kurucz model best able to fit these two requirements is used to give each star's emission across the full wavelength range of each filter ( $F_\lambda$ ), and at  $5556 \text{ \AA}$  ( $F_{5556\text{\AA}}$ ). The stellar irradiance at each wavelength is then scaled to an absolute emission ( $F_S(\lambda)$ ) to account for the different distances of the target stars, achieved by using Vega as the standard star. Recently Bohlin et al. (2014) determined the absolute irradiance of Vega at  $5556 \text{ \AA}$  to be  $3.44e-9 \text{ erg s}^{-1} \text{ cm}^{-2} \text{ \AA}^{-1}$ . Vega is defined to be 0 magnitude in the  $V_J$  band, so the absolute emission of each star at wavelength  $\lambda$  is given by Eq. (3).

$$F_S(\lambda) = \frac{F_\lambda}{(F_{5556\text{\AA}})} (3.44e^{-9}) (10^{(V_J/-2.5)}) \quad (3)$$

This absolute energy flux is then converted to a photon flux ( $F_n$ ), using the relationship  $F_n(\lambda) = F_S(\lambda)/(hc/\lambda)$ , where  $h$  is the Planck constant and  $c$  is the speed of light. The final step is to

take this photon flux and determine what fraction of these photons are able to hit the MVIC detector. This final flux,  $F_e$ , gives the count rate from a given star as predicted by the pre-flight calibration. It is calculated as a function of the detector response ( $\chi$ ), the size of the circular telescope aperture ( $3.75 \text{ cm}^2$  radius, Reuter et al., 2008) and the gain (58.6 photoelectrons/DN), according to  $F_e = (\pi 3.75^2/58.6) \int^{h\nu} F_n(\lambda) \chi(\lambda) d\lambda$ . This count rate can now be directly compared to that observed.

#### 2.4. Star photometry

For each star, we perform basic aperture photometry to measure the total flux and its associated uncertainty (in counts) of both the star and the surrounding sky using the IDL routine `basphote.pro` (Buie, 2015). This measurement is achieved by using the image's exposure time, and by assuming a read-out noise of 30 electrons, a gain of 58.6 photoelectrons per DN (Reuter et al., 2008), a sky annulus between 10 and 20 pixels, and an aperture size of 4 pixels (to allow for smearing). The results from this routine were checked against other standard photometry algorithms (e.g. `aper.pro` see Buie, 2015), and the results were found to be consistent.

#### 2.5. Stellar calibration consistency

In each observation sequence the TDI arrays take only one image of a given target; however, Pan Frame usually takes between

**Table 6**

List of the adjustment factors and their error of the mean (AF) required to correct the observed to predicted counts rate, where the predicted count rates = (observed count rates  $\times$  adjustment factor) using all the stars observed. The number of stars given is the total number of stars found in all the calibration images taken by each filter, minus those considered to be outliers by the robust mean (as given by the value inside the parentheses). \*Charon-based red channel adjustment factor is set by the stellar calibration.

Filter and pivot wavelength	Both AF	Side 0 AF	Side 1 AF	Both #stars	Side 0 #stars	Side 1 #stars	Charon AF
Blue 492 nm	$1.00 \pm 0.01$	$1.02 \pm 0.01$	$0.99 \pm 0.01$	289 [35]	140 [9]	149 [26]	1.02
Red 624 nm	$1.21 \pm 0.01$	$1.23 \pm 0.01$	$1.21 \pm 0.01$	502 [119]	251 [18]	313 [39]	1.21*
NIR 861 nm	$1.32 \pm 0.01$	$1.38 \pm 0.02$	$1.27 \pm 0.01$	345 [60]	121 [22]	225 [37]	1.39
CH4 883 nm	$1.46 \pm 0.02$	$1.44 \pm 0.04$	$1.51 \pm 0.03$	79 [23]	19 [4]	67 [12]	1.56
Pan 1692 nm	$1.17 \pm 0.01$	$1.27 \pm 0.01$	$1.13 \pm 0.01$	571 [65]	139 [18]	430 [49]	NA
Pan 2692 nm	$1.22 \pm 0.01$	$1.23 \pm 0.01$	$1.21 \pm 0.01$	455 [73]	272 [41]	182 [33]	NA
Pan frame 692 nm	$1.26 \pm 0.01$	$1.28 \pm 0.01$	$1.23 \pm 0.01$	594 [74]	210 [18]	385 [55]	NA

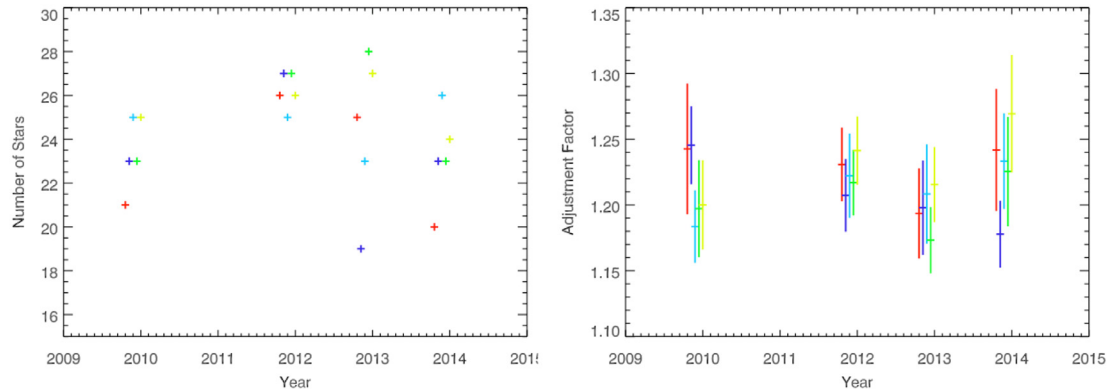


**Fig. 3.** The number of stars (left) and the adjustment factor derived (right) from Pan Frame observations of NGC 6406 and 6475. The colors indicate results from the different images taken in a given observation sequence, and correspond between the two figures.

2 and 6 images (see Table 5). Thus, the Pan Frame images can be used to determine the consistency of our stellar calibration pipeline between different images of the same target in a single observing sequence (i.e. over minute/hourly timescales) and different observing sequences (i.e. over yearly timescales). The targets most often observed are the galaxy clusters NGC 6405 and 6475, and thus they are the focus of this study. Fig. 3 shows the number of stars detected in each image of NGC 6405 and 6475 that could be correlated to ones in the Tycho catalog. As the figure shows the number of stars observed in different images in a single observing sequence does vary, but only by a few stars (maximum is  $\pm 5$ ). Furthermore, there is not a systematic temporal trend in their variation between different observing sequences. The adjustment factor derived from these observations is also shown in Fig. 3 (i.e. the required factor to go from the count rates predicted by the preflight calibration to those observed). The results show that all observations of these galaxy clusters result in very similar adjustment values (almost the same within error). Thus we conclude that our analysis technique provides a consistent way of deriving the required calibration adjustment factor at both short- and long-timescales, at least for Pan Frame images. The TDI filters also display long-term stability in the derived adjustment factor (see the discussion in Section 3), but it is not possible with our current data set to confirm their stability on shorter timescales.

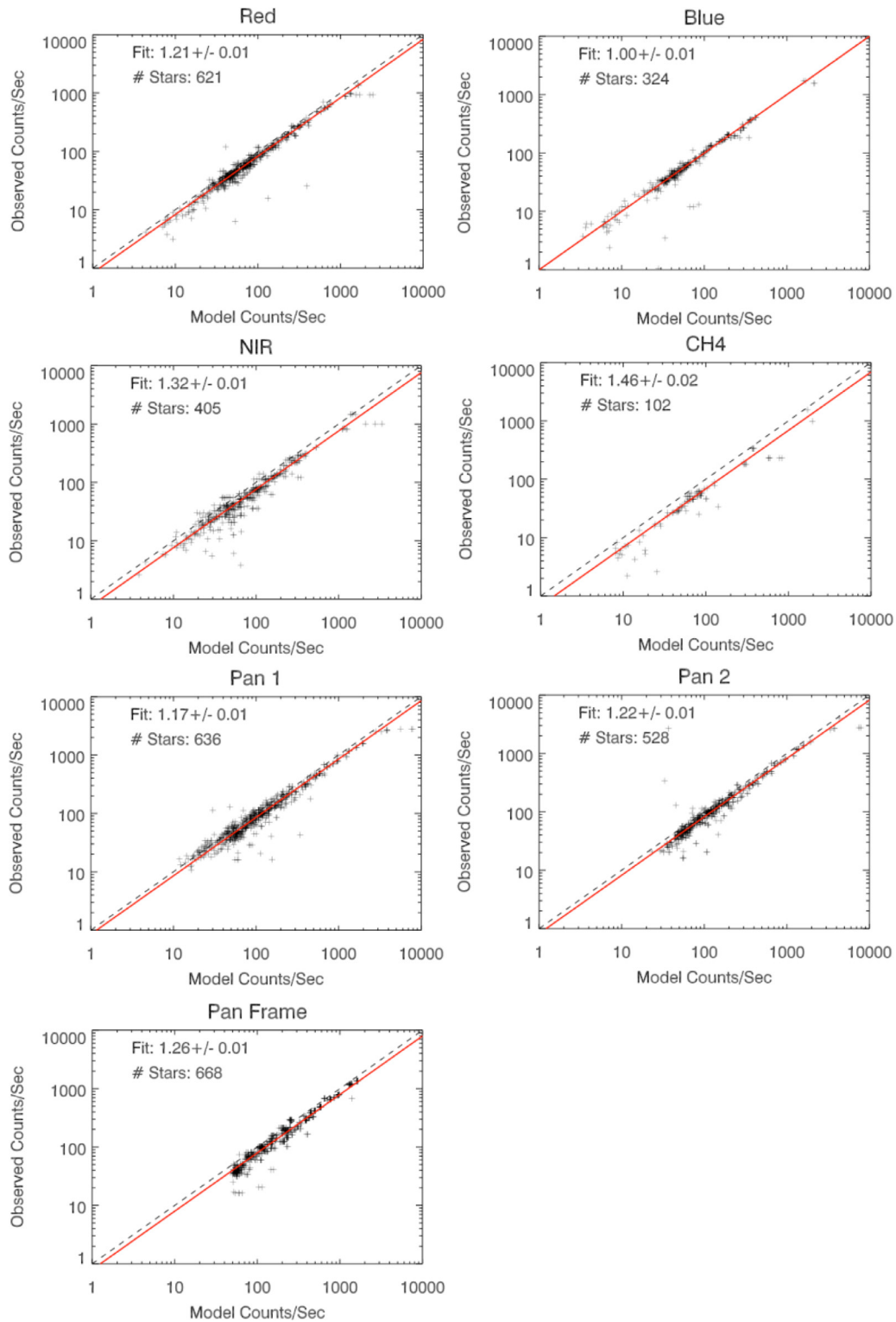
## 2.6. Stellar calibration results

Fig. 4 compares the observed and predicted count rates for all observations made with each of the MVIC detectors. The line of best fit to the data (shown in red) provides the required adjustment factor to go from the count rates predicted by the preflight calibration to those observed. It was determined by finding the robust mean of all the data points shown. This technique provides a systematic method of removing statistically outlying points, which

are defined here as those outside of two standard deviations from the mean. Table 6 gives the total number of stars identified in the calibration images taken by each filter, along with the number of stars that were considered outliers and removed (typically between 5 and 15% of the total number of stars identified). These outliers are assumed to be stars we have incorrectly identified, although other explanations are also possible. The (robust mean) adjustment values for each of the detectors are listed in Table 6, along with the error of the mean (i.e. the standard deviation of the robust mean divided by the root of the number of points, note this is how error values are defined henceforth). As the Table shows, the calibration error is  $\leq 1\%$  for all filters, except the CH4 filter. The CH4 filter has a low throughput, leading to a smaller number of stars being observed and therefore a higher error (1.4%). Thus this work either meets or is better than the 1% inflight radiometric calibration error predicted by Reuter et al. (2008) for all filters except CH4 (which is only slightly worse). The close agreement of the model and observed star counts implies that the computer routine developed (known as correlate stars) is correctly identifying the stars in the images in most cases.

## 3. The effect of the electronics side on MVIC images

On approach to Pluto it was observed that the gain of the NIR channel drifted if the output was read through the primary electronics side (known as side 1), whilst it remained stable when read through the backup electronics side (side 0). During New Horizons' cruise to the Pluto system MVIC's annual checkout observations were alternated between electronic sides, but this effect was not discovered primarily because there were too few observations taken on each electronic side to make finding robust trends possible. This problem with the NIR channel was not discovered during New Horizons' 2007 encounter with Jupiter because all science observations were taken using the same electronic side (side



**Fig. 4.** Plots of the predicted versus the observed counts/second for all observations made with each MVIC filter. The black dotted line shows  $x=y$ , and the red solid line shows the best fit, as given in each of the figures and Table 6. The total number of stars (crosses) is also given in each of the figures. (For interpretation of the references to color in this figure legend, the reader is referred to the web version of this article.)

1). However, upon approach to the Pluto system observations were made using alternating electronics sides, and by systematic inspection of Charon's color in the NIR the gain drift became apparent.

Thus, it was important to check whether this gain fluctuation affected the adjustment factors required to correct the count rates predicted by the preflight calibration to those observed for all the

MVIC detectors. Figs. 5 and 6 show the model versus observed count rates for observations made only with side 0 or side 1. These results are summarized in Fig. 7 and Table 7, which show that most of the detectors do not show a significant change in adjustment factor with electronic side. The close agreement of the adjustment values for Pan Frame and Pan 2 detectors in Fig. 7

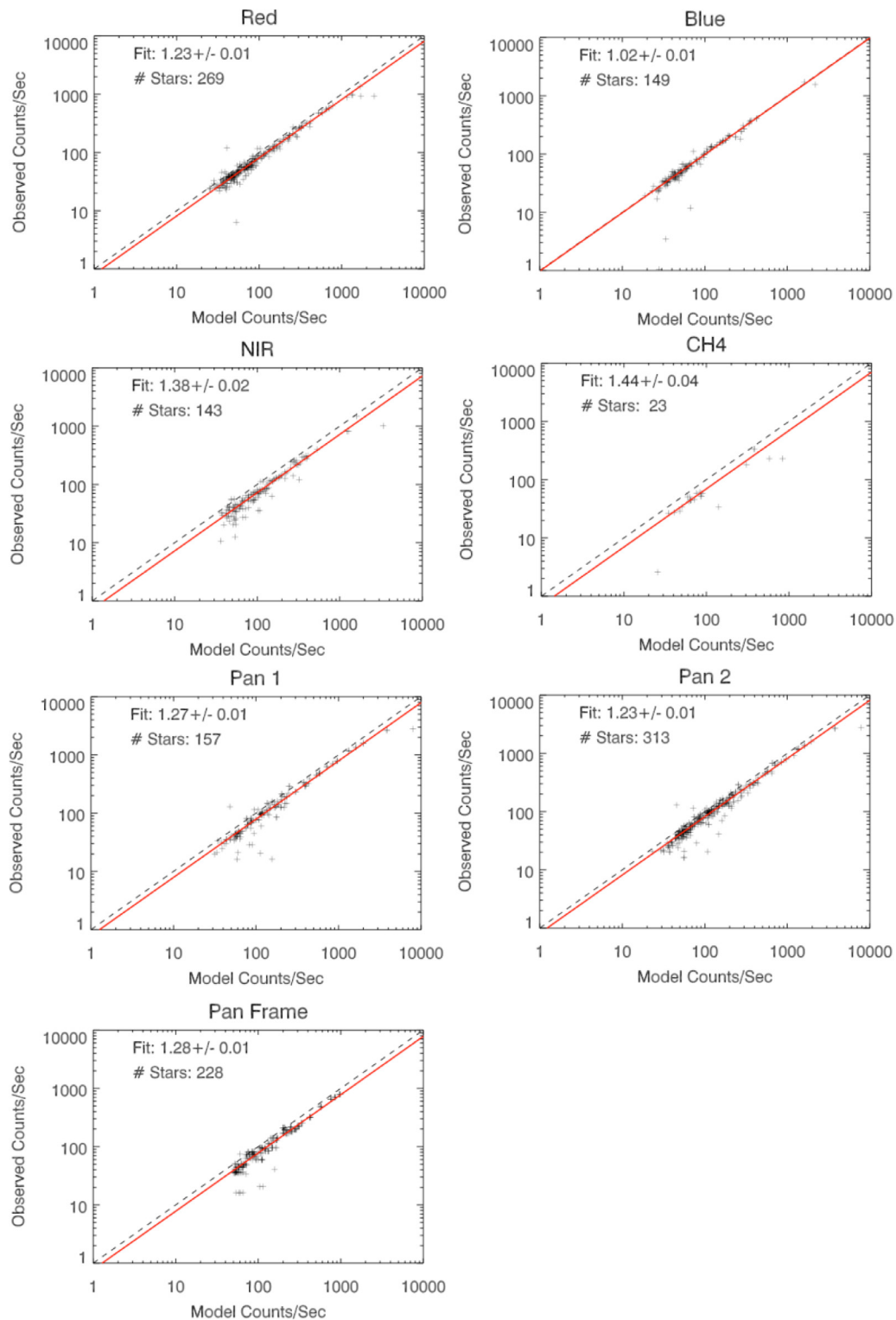


**Fig. 5.** Plots of the predicted versus the observed counts/second for all observations made on the electronics side 0 with each MVC filter. The black dotted line shows  $x = y$ , and the red solid line shows the best fit, as given in each of the figures and Table 5. The total number of stars (crosses) is also given in each of the figures. (For interpretation of the references to color in this figure legend, the reader is referred to the web version of this article.)

provides confidence that the derived values are correct, since they cover the same wavelength range but have been independently derived. The two detectors that show notable change in their adjustment values with electronic sides are the NIR and Pan 1 detector. This problem with Pan 1 was first discovered during the instrument's commissioning phase in 2006, which was early enough

to be able to mitigate the problem by ensuring all science observations were taken using side 1 of Pan 1. However, because the problem with the NIR channel was not known until shortly before encounter, similar mitigation steps were not enacted for it. Therefore, post-observation processing solutions had to be used instead, as described in the next section.

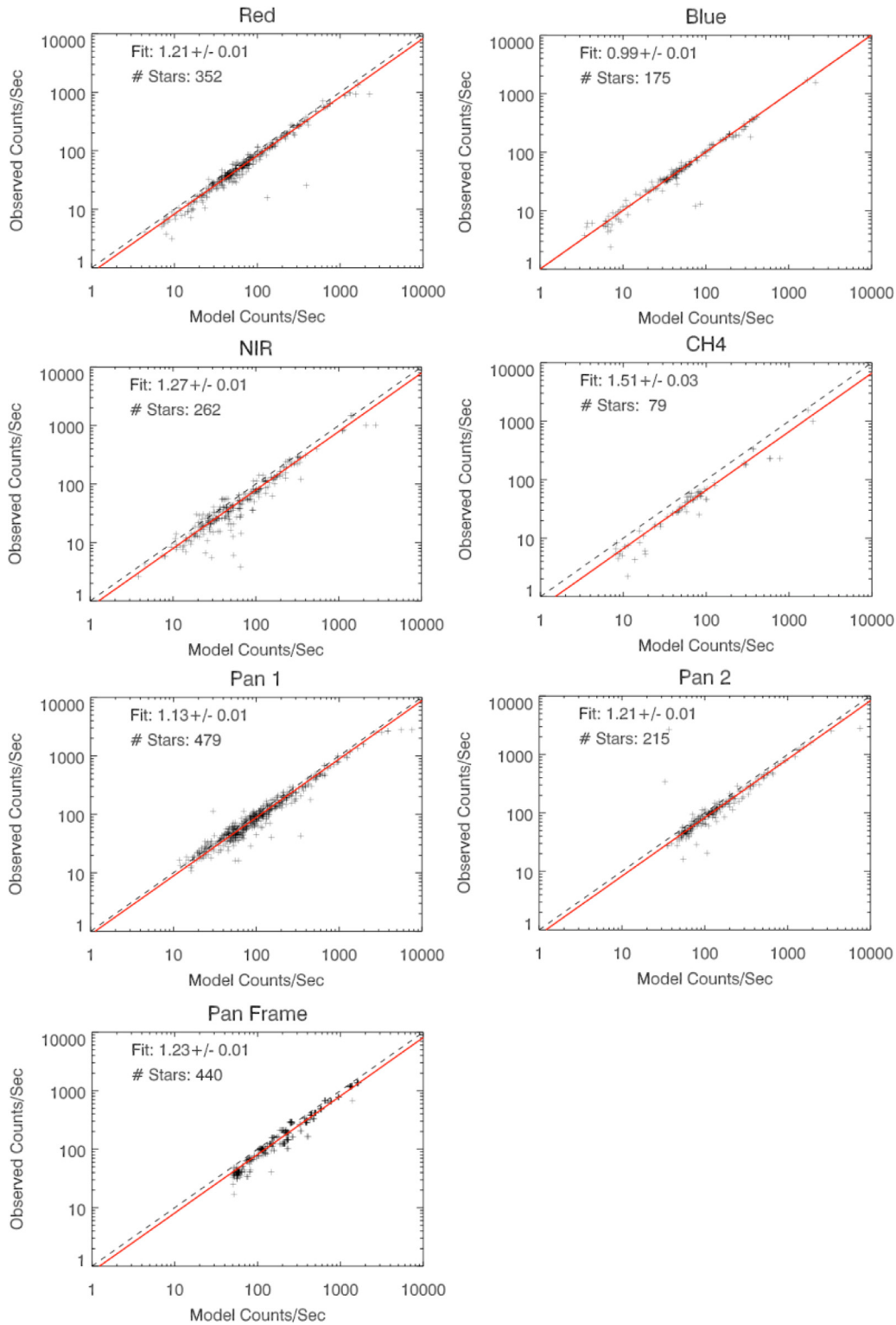


**Fig. 6.** Plots of the predicted versus the observed counts/second for all observations made on the electronics side 1 with each MVIC filter. The black dotted line shows  $x = y$ , and the red solid line shows the best fit, as given in each of the figures and Table 5. The total number of stars (crosses) is also given in each of the figures. (For interpretation of the references to color in this figure legend, the reader is referred to the web version of this article.)

Fig. 7 also shows that there is significant difference in the adjustment factors between detectors. The Blue channel requires negligible adjustment ( $1.00 \pm 0.01$ ), whilst the NIR and CH4 channels require a  $\sim 20$  to 45% correction respectively, with the other channels lying between these extremes. It is unclear why these two channels require the most correction. Although it is worth noting

that the wavelength range of the CH4 filter (860–910 nm) is much narrower than the other filters (see Fig. 1), so fewer stars are observed its images (see Tables 6 and 7) leading to higher errors (up to 4%) in its adjustment value.

Since the cause of the problems with NIR and Pan 1 channels are not understood, it was possible they could vary over time.

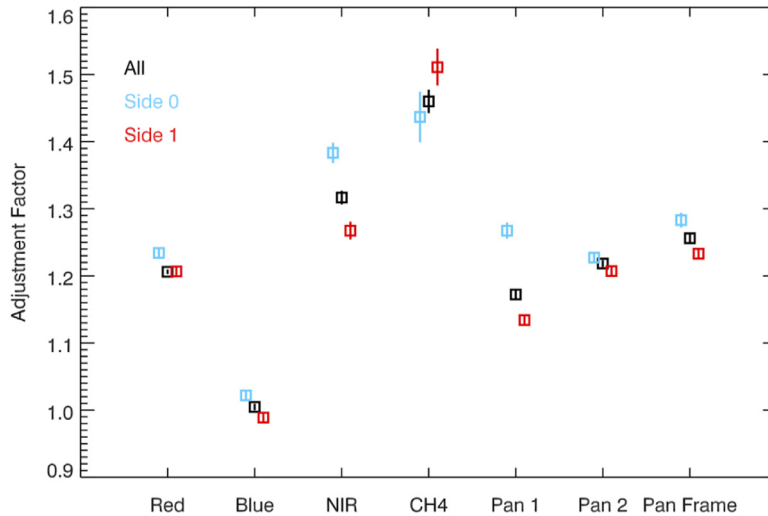


Fig. 7. The adjustment ratio of all MVIC filters, as calculated for all electronic sides, just side 0 and just side 1.

Table 7

List of the adjustment factors required to correct the observed to predicted counts rate (see Table 6 for more details) using all stars observed each year.

Year	Adjustment factor			Number of stars		
	All	Side 0	Side 1	All	Side 0	Side 1
<b>Red</b>						
2008	1.23 ± 0.01	1.23 ± 0.01	–	61	61	–
2010	1.20 ± 0.02	–	1.20 ± 0.02	98	–	98
2012	1.21 ± 0.02	1.21 ± 0.02	–	77	77	–
2013	1.21 ± 0.01	–	1.21 ± 0.01	113	–	113
2014	1.21 ± 0.01	1.24 ± 0.01	1.21 ± 0.01	272	131	141
<b>Blue</b>						
2008	0.99 ± 0.01	0.99 ± 0.01	–	36	36	–
2010	0.97 ± 0.01	–	0.97 ± 0.01	47	–	47
2012	1.00 ± 0.01	1.00 ± 0.01	–	41	41	–
2013	1.01 ± 0.01	–	1.01 ± 0.01	51	–	51
2014	1.02 ± 0.01	1.05 ± 0.01	1.00 ± 0.02	149	72	77
<b>NIR</b>						
2008	1.46 ± 0.03	1.46 ± 0.03	–	40	40	–
2010	1.18 ± 0.02	–	1.18 ± 0.02	86	–	86
2012	1.46 ± 0.06	1.46 ± 0.06	–	42	42	–
2013	1.42 ± 0.03	–	1.42 ± 0.03	52	–	52
2014	1.30 ± 0.01	1.34 ± 0.02	–	185	61	124
<b>CH4</b>						
2008	1.45 ± 0.05	1.45 ± 0.05	–	12	12	–
2010	1.48 ± 0.07	–	1.48 ± 0.07	17	–	17
2012	1.42 ± 0.06	1.42 ± 0.06	–	11	11	–
2013	1.53 ± 0.05	–	1.53 ± 0.05	17	–	17
2014	1.51 ± 0.04	–	1.51 ± 0.04	45	–	45
<b>Pan 1</b>						
2008	1.28 ± 0.02	1.28 ± 0.02	–	91	91	–
2010	1.25 ± 0.02	–	1.25 ± 0.02	70	–	70
2012	1.25 ± 0.02	1.25 ± 0.02	–	66	66	–
2013	1.28 ± 0.01	–	1.28 ± 0.01	147	–	147
2014	1.02 ± 0.01	–	1.02 ± 0.01	262	–	262
<b>Pan 2</b>						
2008	1.24 ± 0.02	1.24 ± 0.02	–	97	97	–
2010	1.20 ± 0.02	–	1.20 ± 0.02	83	–	83
2012	1.26 ± 0.02	1.26 ± 0.02	–	86	86	0
2013	1.23 ± 0.01	–	1.23 ± 0.01	132	–	132
2014	1.18 ± 0.01	1.18 ± 0.01	–	130	130	–
<b>Pan frame</b>						
2008	1.31 ± 0.01	1.31 ± 0.01	–	22	22	–
2010	1.22 ± 0.02	–	1.22 ± 0.02	124	–	124
2012	1.28 ± 0.01	1.28 ± 0.01	–	206	206	–
2013	1.20 ± 0.01	–	1.20 ± 0.01	129	–	129
2014	1.32 ± 0.01	–	1.32 ± 0.01	187	–	187

Therefore, the adjustment factor was determined for each filter for each year, as shown in Fig. 8. This was possible because, although all Pan 1 science observations were made using the electronic side 1, annual checkout observations were made on both sides to monitor the problem. Fig. 8 shows that for all detectors (except the two detectors that are known to problematic: NIR and Pan 1) that the adjustment factors either agree within error every year or very nearly do so, leading to the conclusion that there is no drift in the calibration with time. Furthermore, there are no obvious temporal dependence trends in the NIR and Pan 1 adjustment factors, and their deviations from the average adjustment factor is not increasing with time (if anything the opposite is true for the NIR detector).

#### 4. Charon calibration process

We also derived a channel-wise relative radiometric calibration from Charon observations for the Blue, NIR, and CH4 channels, scaled from the Red channel stellar calibrations (independent of the previously described stellar calibration) The disk-averaged color ratios of Charon were matched to those that would be produced by the product of a parametric synthetic reflection spectrum (normalized to a mean F555W geometric albedo of 0.41, Buratti et al. (2016)) and a solar spectrum that also reproduces the global color ratios of Charon as measured by the Hubble Space Telescope's (HST) ACS HRC in the F435W and F555W filters (Buie et al., 2006).

Since Charon is broadly characterized by two latitudinally-controlled color units (neutral mid-latitudes and a red polar cap), the relative contributions of these two color units was adjusted in order to match the orientation of Charon as observed by HST between 2002 and 2003. We found that this geometric correction to the global color ratios of Charon was negligible. Note, the details of C\_COLOR2 and all other observations discussed in this section and the ones that follow are given in Table 8.

The parametric reflection spectrum that we adopted in order to reproduce the Buie et al. (2006) Charon colors had the form

$$p(\lambda) = (1 + e^{0.495 - 2.43 \times 10^{-4} \lambda})^{-1}, \quad (4)$$

with  $\lambda$  in nm.

Correction factors relative to the Red channel were determined for Blue, NIR, and CH4 channel transmission curves as follows:

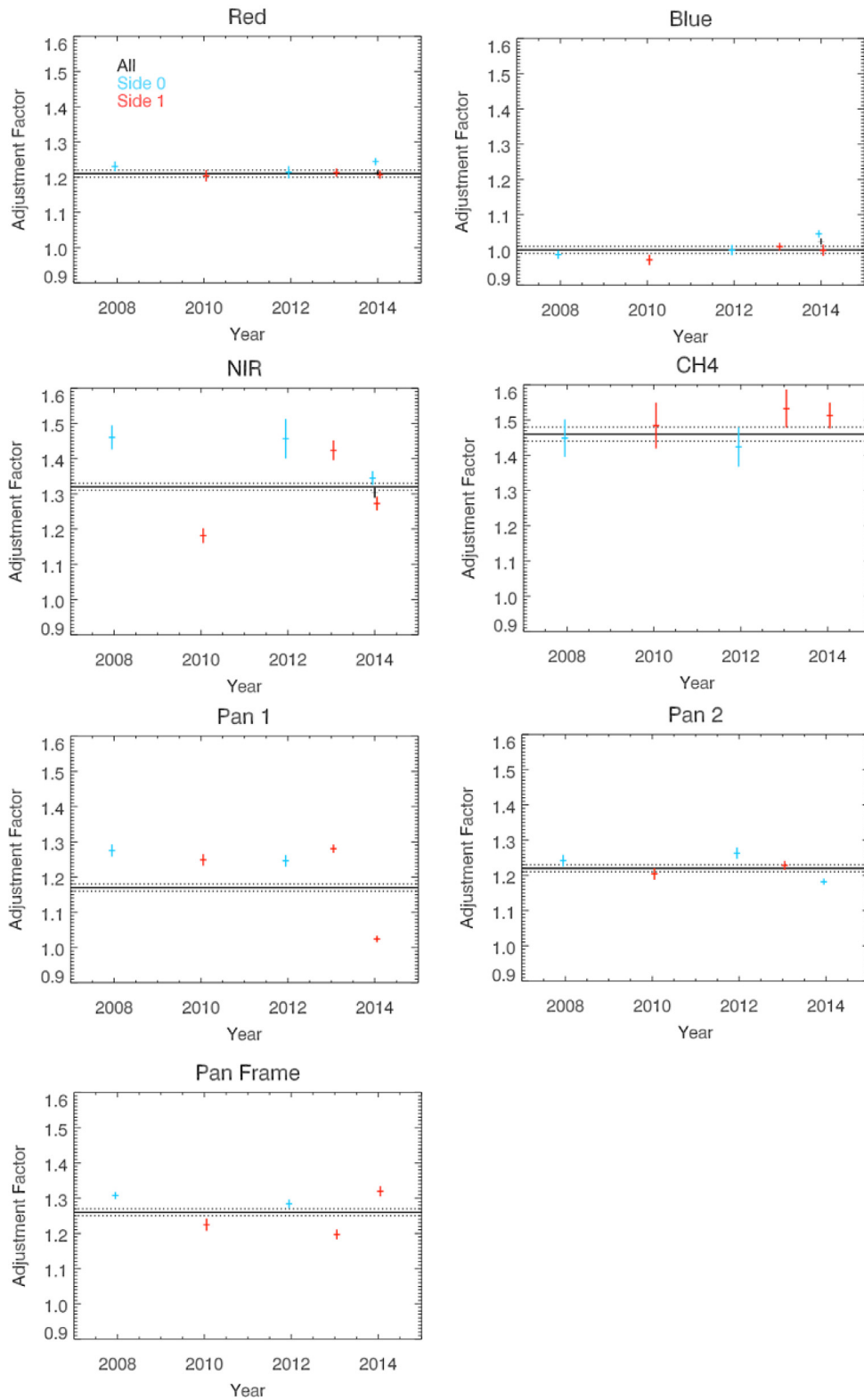


**Fig. 8.** The adjustment ratio of all the MVIC filters plotted by year, as calculated for all electronic sides, just side 0 and just side 1 where available. The black solid and dotted lines shows the adjustment value and the error of the mean for each filter, which was derived from all available data as given in Table 5.

**Table 8**  
Details of the observations used in the “Charon” calibration.

Observation name	Target	Mid-observation time (UTC)	Onboard mission elapsed time (MET)	Phase (degrees)	Electronic side
PC_MULTI_MAP_B17	Pluto and Charon	13-July-2015 03:38:06	0299064592	Pluto:15.6 Charon:15.5	0
C_COLOR2	Charon	14-Jul-2015 10:42:28	0299176432	38.6	0
P_COLOR_2	Pluto	14-Jul-2015 11:10:52	0299178092	38.8	1

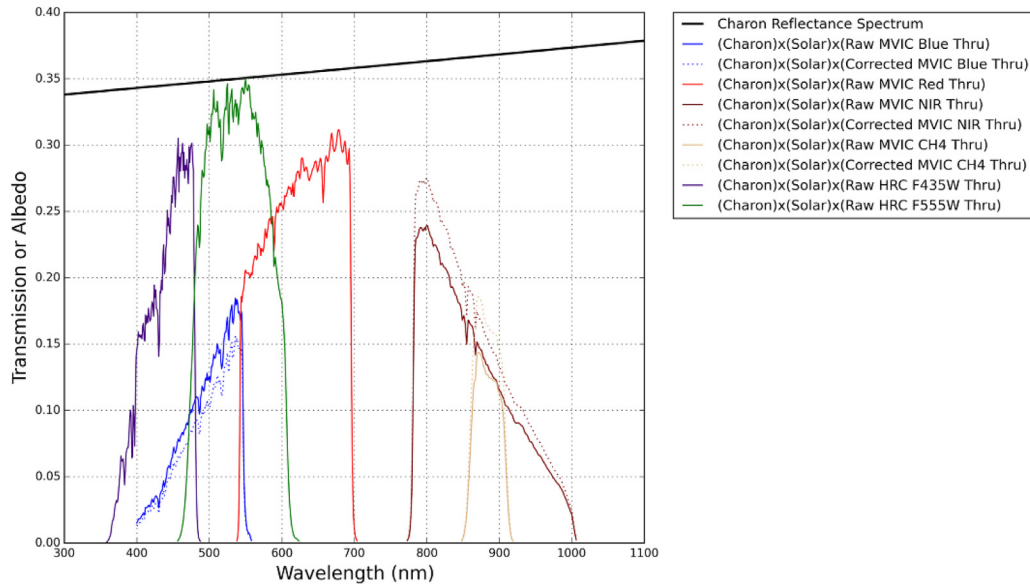


**Fig. 9.** Raw input and calibrated transmission curves (scaled by product of solar spectrum and model Charon spectrum) for Charon-based calibration procedure, and derived parametric Charon reflectance spectrum (geometric albedo, black line). HST ACS HRC F435W and F555W filters accessed from <http://www.stsci.edu/hst/acs/analysis/throughputs> on October 29, 2015.

- (1) The global mean flux of C\_COLOR2 images, with regional contributions reweighted to correct them to HST's viewing geometry, were calculated for Red, Blue, NIR, and CH4 channels.
- (2) The observed ratios of Blue, NIR, and CH4 to Red were determined.
- (3) The predicted ratios of Blue, NIR, and CH4 to Red were determined by integrating the product of the solar spectrum, the parametric HST Charon reflection spectrum (Eq. (4)), and each filter's response curve over wavelength.
- (4) The ratio of the predicted ratio over the observed ratio was adopted as the *relative* throughput correction factor for Blue, NIR, and CH4. These and the Red channel were all scaled by the *absolute* correction factor (Table 6) derived for the Red channel from the stellar calibrations.

## 5. Charon calibration results

The throughput curves used in this analysis before and after correction, as well as the parametric Charon spectrum, are illustrated in Fig. 9. The Charon-based calibrations produce results very similar to the stellar calibrations, demonstrating a cross-validation of the two unique approaches. The largest variation between the two calibration solutions was in the CH4 channel, for which the Charon-based calibration determined a correction factor 3–7% larger (depending on power side) than the stellar calibrations. This channel has the pivot wavelength farthest from the pivot wavelengths of the two HST filters used to calibrate the parametric Charon reflectance spectrum, and it is not surprising that this is where the largest difference between the two calibration approaches appeared.

## 6. Bootstrapping a power side correction

The calibration solution for images affected by the electronics-side-dependent gain drift includes the derivation of a correction for affected channels using repeated imagery of the same terrains. This “bootstrapping” process has proven to be very effective for the flyby data, as the Pluto system contains two excellent calibration targets. The first is Charon, which has little to no longitudinal color variations and provides an excellent “gray card” for

approach imagery where both Pluto and Charon are visible in a single MVIC FOV. The second is informally called Sputnik Planum, which is a large and flat region that is extremely uniform in color and albedo and which is visible at high resolution in the imagery where Charon is not available.

For a given image set affected by gain drift, the following process is used to derive a bootstrap correction: (1) identify the temporally-nearest image set not affected by gain drift that contains overlapping imagery of either Sputnik Planum or Charon; (2) co-register the imagery on a map grid; (3) extract pixels from a contiguous region of equal surface area from both image sets within either Sputnik Planum or the disk of Charon; (4) determine the summed flux within these pixels in the Red channel and the channel of interest  $i$ ; (5) compute the ratio of these summed fluxes between the channel of interest  $i$  and the Red channel in both image sets; and (6) compute the ratio of these two ratios, which is the correction factor:

$$CF_i = \left( \left( \frac{\sum F_{i,SIDE 0}}{\sum F_{Red,SIDE 0}} \right) / \left( \frac{\sum F_{i,SIDE 1}}{\sum F_{Red,SIDE 1}} \right) \right) \quad (5)$$

For consistency, all channels except Red (which serves as our control channel and does not appear to be affected by gain drift) are corrected in this way, though the derived NIR correction is always substantially larger than those derived for Blue or CH4. What follows is a worked example for P\_COLOR\_2, which was taken on side 1 of the electronics and was therefore subject to gain drift. In this example we chose PC\_MULTI\_MAP\_B17 as the control imagery, as it was taken on side 0 of the electronics (which is not subject to gain drift) and it covered a similar sub-spacecraft longitude and shows Sputnik Planum clearly.

The images were extracted to an interim common map projection, and a circular region (on the sphere) with a radius of  $10^\circ$  was extracted from the core of Sputnik Planum at approximately  $20^\circ$  North,  $180^\circ$  East in both images. In this region, the median raw Red/NIR DN ratio for P\_COLOR\_2 was 0.766, while for PC\_MULTI\_MAP\_B17 it was 0.815; the ratio of these two determines the bootstrapped NIR gain correction factor for P\_COLOR\_2, 1.064. This correction factor was found to be insensitive to whether ratios were determined from mean color ratios, median color

ratios, or the ratios of areal sums (the latter being adopted). For P\_COLOR\_2, derived gain correction factors for Blue (1.039) and CH4 (1.019) were substantially smaller.

To test for robustness, the maps were intentionally misregistered by up to 5° North and South, the extracted radius shrunk to 5°, and the bootstrapping process repeated. This keeps the region of interest within the boundaries of Sputnik Planum, but incorrectly correlates different regions within Sputnik Planum. Due to the uniformity of Sputnik Planum's colors on large spatial scales, the derived correction ratios varied by only small amounts (~1%), demonstrating that the corrections are robust to small misregistration between image sets if Sputnik Planum is used as a control region. Charon provides similar robustness due to its longitudinal color uniformity.

## 7. Radiometric calibration keywords

To transform DN detected by MVIC into physical units describing the incoming spectral energy distribution, MVIC image headers contain two calibration-dependent keywords. For the first Planetary Data System (PDS) release, these keywords are defined based on the stellar calibrations described in this document. The diffuse source sensitivity keywords are defined as:

$$R_{TARGET,FILTER} = \int_0^{\infty} \frac{S_{R\_TARGET}(\lambda) \chi_{TARGET}(\lambda) A \lambda \Theta}{S_{R\_TARGET}(\lambda_{p,FILTER}) h c e^{-} / DN} d\lambda,$$

while the point-source sensitivity keywords are defined as

$$P_{TARGET,FILTER} = \int_0^{\infty} \frac{S_{P\_TARGET}(\lambda) \chi_{TARGET}(\lambda) A \lambda}{S_{P\_TARGET}(\lambda_{p,FILTER}) h c e^{-} / DN} d\lambda.$$

In these equations  $S_{P\_TARGET}(\lambda)$  is a source-dependent spectrum for a point source target in  $erg\ s^{-1} cm^{-2} \text{\AA}^{-1}$ , and  $S_{R\_TARGET}(\lambda)$  is a source-dependent spectrum for an extended source target in  $erg\ s^{-1} cm^{-2} \text{\AA}^{-1} sr^{-1}$ , where  $\text{\AA}$  is the wavelength in angstroms and  $sr$  is steradians.  $\chi_{FILTER}(\lambda)$  is the responsivity, which is the same as previously described except it uses the filter transmission curves for a specific filter after throughput is corrected by the adjustment factors from Table 6,  $\lambda_{p,FILTER}$  is the pivot wavelength of a specific filter,  $A$  is the aperture collecting area in  $cm^2$  for the MVIC telescope,  $\frac{e^{-}}{DN}$  is the mean MVIC gain, and  $\Theta$  is the MVIC pixel IFOV in steradians ( $19.77\ \mu rad$  by  $19.77\ \mu rad$ , Reuter et al., 2008). These keywords are defined for SOLAR, PLUTO, CHARON, JUPITER, and PHOLUS target spectra. The units for an extended target are  $(DN/s)/(erg/cm^2/s/\text{\AA}/sr)$ , and for a point source the keyword units are  $(DN/s)/(erg/cm^2/s/\text{\AA})$ . The spectra used to define these keywords are derived from the following sources: Charon (Buie and Grundy, 2000), Jupiter (Spencer et al., 2004), Pluto (Douté et al., 1999), Pholus (Cruikshank et al., 1998) and Solar (Colina et al., 1996). The actual spectra used will be delivered to the PDS as part of the next delivery by the New Horizons project; some have been slightly updated.

## 8. Conclusion

We have described the two semi-independent methods used to calibrate New Horizons' MVIC instrument. The close agreement be-

tween the two methods provides reassurance that both are functioning correctly. The "Charon" calibration was used to make science products widely throughout New Horizons' encounter with Pluto. However, the stellar calibration will be used in future PDS deliveries primarily because it was produced for all color filters and does not rely on having a known color target in the field of view. We also describe a previously known problem with the Pan 1 filter, and the observational strategy adopted to minimize its effect. Finally we have also described the newly discovered gain problem with the NIR detector and the bootstrapping technique that has been adopted to mitigate it.

## Acknowledgments

This work was supported by NASA's New Horizons Project. S. Philippe and B. Schmitt acknowledge the Centre National d'Etudes Spatiales (CNES) for its financial support through its "Système Solaire" program.

## References

- Bohlin, R.C., 2014. Hubble space telescope CALSPEC flux standards: Sirius (and Vega). *Astron. J.* 147 (6), 127.
- Buie, M.W., Grundy, W.M., 2000. The distribution and physical state of H<sub>2</sub>O on Charon. *Icarus* 48, 324–339.
- Buie, M.W., Grundy, W.M., Young, E.F., Young, L.A., Stern, S.A., 2006. Orbits and photometry of Pluto's satellites: Charon, S/2005P1, and S/2005 P2. *Astron. J.* 132, 290–298.
- Buie, M.W., 2015. General Purpose IDL Functions and Procedures <http://www.boulder.swri.edu/~buie/idl/pro/>.
- Burrati, B.J., Hofgartner, J.D., Hicks, M.D., Weaver, H.A., Stern, S.A., Momary, T., Mosher, J.A., Beyer, R.A., Young, L.A., Ennico, K., Olkin, C.B., 2016. Global Albedos of Pluto and Charon from LORRI New Horizons observations. *Icarus* Submitted.
- Cruikshank, D.P., Roush, T.L., Bartholomew, M.J., Geballe, T.R., Pendleton, Y.J., White, S.M., Bell II, J.F., Davies, J.K., Owen, T.C., de Bergh, C., Tholen, D.J., Bernstein, M.P., Brown, R.H., 1998. The composition of Centaur 5145 Pholus. *Icarus* 135, 389–407.
- Douté, S., Schmitt, B., Quirico, E., Owen, T.C., Cruikshank, D.P., de Bergh, C., Geballe, T.R., Roush, T.L., 1999. Evidence for methane segregation at the surface of Pluto. *Icarus* 142, 421–444.
- Colina, L., Bohlin, R.C., Castelli, F., 1996. The 0.12–2.5  $\mu m$  absolute flux distribution of the sun for comparison with solar analog stars. *Astron. J.* 112, 307–315.
- Grundy, W.M.31 co-authors, 2016. Surface compositions across Pluto and Charon. *Science* In Press.
- Hog, E., Fabricius, C., Makarov, V.V., Urban, S., Corbin, T., Wycoff, G., Bastian, U., Schwekendiek, P., Wicenc, A., 2000a. The Tycho-2 catalogue of the 2.5 million brightest stars. *A&A* 355, L27.
- Hog, E., Fabricius, C., Makarov, V.V., Bastian, U., Schwekendiek, P., Wicenc, A., Urban, S., Corbin, T., Wycoff, G., 2000b. Construction and verification of the Tycho-2 catalogue. *A&A* 357, 367.
- Hog, E., Fabricius, C., Makarove, V.V., Urban, S., Corbin, T., Wycoff, G., Bastian, U., Schwekendiek, P., Wicenc, A., 2000c. Guide to the Tycho-2 Catalogue <http://www.astro.ku.dk/~erik/Tycho-2/>.
- Kurucz, R.L., 1993. A new opacity-sampling model atmosphere program for arbitrary abundances. In: Dworetzky, M.M., Castelli, F., Faraggiana, R. (Eds.), *Peculiar Versus Normal Phenomena in A-type and Related Stars*. In: A.S.P. Conference Series, vol. 44, pp. 87–97.
- Laidler, et al., 2005. *Synphot User's Guide*. STScI, Baltimore Version 5.0.
- Reuter, D.C., Stern, S.A., Scherrer, J., Jennings, D.E., Baer, J., Hanley, J., Hardaway, L., Lunsford, A., McMudroch, S., Moore, J., Olkin, C., Parizek, R., Reitsma, H., Sabatke, D., Spencer, J., Stone, J., Throop, H., Van Cleve, J., Weigle, G.W., Young, L.A., 2008. Ralph: a visible/infrared imager for the New Horizons Pluto/Kuiper belt mission. *Space Sci. Rev.* 140, 129–154.
- Spencer, J.R., Carlson, R.W., Becker, T.L., Blue, J.S., 2004. Maps and spectra of Jupiter and the Galilean satellites. In: Bagenal, F., Dowling, T.E., McKinnon, W.B. (Eds.), *Appendix 1 of Jupiter the Planet, Satellites and Magnetosphere*.
- Weaver, H.A.50 co-authors, 2016. The small satellites of Pluto as observed by New Horizons. *Science* In Press.